Cation-Driven Assembly of Bilayered Vanadium Oxide and Graphene Oxide Nanoflakes to Form Two-Dimensional Heterostructure Electrodes for Li-ion Batteries

Ryan Andris¹, Timofey Averianov¹, Michael J. Zachman², Ekaterina Pomerantseva¹*

Keywords: bilayered vanadium oxide; reduced graphene oxide; liquid phase exfoliation; self-assembly; heterostructures; Li-ion batteries

Abstract

Lithium intercalated bilayered vanadium oxide (LVO or δ-Li_xV₂O₅·nH₂O) and graphene oxide (GO) nanoflakes were assembled using a concentrated lithium chloride solution and annealed under vacuum at 200°C to form two-dimensional (2D) δ-Li_xV₂O₅·nH₂O and reduced GO (rGO) heterostructures. We found that the Li-ions from LiCl enhanced the oxide/carbon heterointerface formation and served as stabilizing ions to improve structural and electrochemical stability. The graphitic content of the heterostructure could be easily controlled by changing the initial GO concentration prior to assembly. We found that increasing the GO content in our heterostructure composition helped inhibit the electrochemical degradation of LVO during cycling and improved the rate capability of the heterostructure. A combination of scanning electron microscopy and X-ray diffraction was used to help confirm that a 2D heterointerface formed between LVO and GO, and the final phase composition was determined using energy dispersive X-ray spectroscopy and thermogravimetric analysis. Scanning transmission electron microscopy and electron energy-loss spectroscopy were additionally used to examine the heterostructures at high resolution, mapping the orientations of rGO and LVO layers and locally imaging their interlayer spacings. Further, electrochemical cycling of the cation-assembled LVO/rGO heterostructures in Li-ion cells with non-aqueous electrolyte revealed that increasing the rGO content led to improved cycling stability and rate performance, despite slightly decreased charge storage capacity. The heterostructures with 0, 10, 20, and 35 wt% rGO exhibited capacities of 237, 216, 174, and 150 mAh g⁻¹, respectively. Moreover, the LVO/rGO 35 wt% and LVO/rGO 20 wt% heterostructures retained 75% (110 mAh g⁻¹) and 67% (120 mAh g⁻¹) of their initial capacities after increasing the specific current from 20 mA g⁻¹ to 200 mA g⁻¹, while the LVO/rGO-10 wt% sample

¹ Department of Materials Science and Engineering, Drexel University, Philadelphia, PA 19104

² Center for Nanophase Materials Sciences, Oak Ridge National Laboratory, Oak Ridge, TN 37831, USA

^{*} Corresponding Author: ep423@drexel.edu

retained only 48% (107 mAh g⁻¹) of its initial capacity under the same cycling conditions. In addition, the cation-assembled LVO/rGO electrodes exhibited enhanced electrochemical stability compared to electrodes prepared through physical mixing of LVO and GO nanoflakes in the same ratios as the heterostructure electrodes, further revealing the stabilizing effect of 2D heterointerface. The cation driven assembly approach, explored in this work using Li⁺ cations, was found to induce and stabilize the formation of stacked 2D layers of rGO and exfoliated LVO. The reported assembly methodology can be applied for a variety of systems utilizing 2D materials with complementary properties for applications as electrodes in energy storage devices.

1. Introduction

Vanadium pentoxide has been widely studied in charge storage systems due to its low cost, high redox activity, high energy density, and range of morphologies¹⁻⁵. Moreover, materials with a two-dimensional (2D) morphology and structure are a promising component in technological applications that require the intercalation of charged species, such as sensors, catalysts, and energy storage devices^{6,7}. Layered 2D materials offer open diffusion pathways that facilitate ion transport and approaches to mitigate structural damage from processes that cause material expansion and contraction⁸. Chemically preintercalated bilayered vanadium oxides (BVOs or δ -M_xV₂O₅·nH₂O, where M = Li, Na, K, Mg or Ca) are of particular interest for use in energy storage due to the open layered structure, tunable interlayer spacings greater than 9 Å, and its high oxidation state⁹⁻¹¹. These properties allow δ -M_xV₂O₅·nH₂O to intercalate a relatively large number of ions while undergoing multiple reduction steps. However, transition metal oxides such as BVO are often limited by low electronic conductivity and poor cycling stability^{12, 13}. Therefore, strategies are being explored to improve the electrochemical charge storage properties of BVO and other oxides via the formation of a stable heterointerface with conductive phases such as graphene, carbon nanotubes, conductive carbon precursors, and other carbon-based materials¹⁴⁻¹⁹.

One efficient strategy used to combine 2D materials with complementary properties is a 'top-down' approach. This method requires the exfoliation of two or more dissimilar materials into single-layer or few-layers nanoflakes followed by lamellar assembly into a 2D stacked architecture, called a 2D heterostructure⁸. A characteristic element of the 2D heterostructure is a 2D heterointerface, which is defined as an intimate face-to-face contact between two chemically dissimilar building blocks (structural layers or nanoflakes). However, there is a challenge in assembling the structure so that the different materials gather into alternating layers to form a stable 2D heterointerface without substantial agglomeration of the chemically identical nanoflakes. One strategy that can help control the sequence of the layers is functionalizing the respective nanoflake surfaces with oppositely charged functional groups to induce the heterointerface formation via electrostatic forces^{20,21}. Though the charge-carrying functional group are often large organic molecules that can decrease the electrical conductivity of the functionalized nanoflakes as compared to their pristine state^{20,22}. Further, large functional groups can obstruct the 2D channels between the dissimilar layers and hinder the diffusion of the electrochemically cycled ions. To alleviate some of these challenges, an alternative subset of the 'top-down' approach, described as

cation-driven assembly, is emerging as a possible solution to enhance the heterointerface formation. This technique could also be a potential strategy for prelithiation of Li-ion capacitors²³. This method uses charged ions in a liquid dispersion to induce the assembly of 2D nanoflakes with similar surface charges such as transition metal dichalcogenides, MXenes, and layered MnO₂²⁴⁻²⁹. For example, negatively charged Ti₃C₂T_x and V₂CT_x 2D MXenes were self-assembled into heterostructures using sodium ions, and showed stable volumetric capacitance over 50,000 cycles in a three-electrode aqueous system³⁰. A similar study found that cation-driven assembly drastically improved the long-term stability of delaminated 2D V₂CT_x MXene flakes²⁷. Moreover, this method was used to form a porous MnO₂ framework from 2D nanoflakes for improved Li-ion and Na-ion storage²⁸. While this assembly process could also be used to overcome the low electronic conductivity limitation of metal oxides by integrating conductive layers⁸, no reports have yet shown the experimental realization of this approach. For practical applications, the optimal amount of conductive nanoflakes must be found to form 2D heterostructures with the best properties. To obtain an ideal heterostructure in which nanoflakes of the two constituent materials would alternate, previous studies applied an area-matching model to determine the theoretical molar ratio that would lead to the dominating heterointerface formation rather than re-stacking of identical nanoflakes²¹. However, when synthesizing electrodes for energy storage applications, a balance needs to be found between achieving higher electronic conductivity and maintaining high specific capacities, as the conducting nanoflakes may not necessarily be redox active. Therefore, the ratio between the components of a 2D heterostructure that leads simultaneously to a stable high capacity and rate capability needs to be determined.

Utilizing a 'top-down' 2D heterostructure assembly method in liquid media requires that both materials are prepared as a nanoflake suspension using liquid phase exfoliation (LPE). LPE is an efficient method to divide bulk 2D materials into monolayer or few-layer thick nanoflakes³¹⁻³³. The LPE of δ-Li_xV₂O₅·*n*H₂O was first demonstrated in N-methyl-2-pyrrolidone (NMP) where probe sonication was used to create a suspension of LVO nanoflakes³⁴. The nanoflakes were collected via vacuum filtration, and scanning transmission electron microscopy revealed that LPE induced a morphology change from crumpled sheets to flexible hierarchically arranged nanoflakes with enhanced electronic conductivity. However, integrating LVO nanoflakes exfoliated in NMP with other 2D materials can be a challenge due to the small yield and solvent compatibility limitations. Many 2D conductive materials and their precursors (e.g., MXenes³⁵ and graphene

oxide (GO)³⁶) disperse effectively in water. Therefore, the exfoliation of LVO was also achieved in an aqueous solution with an improved yield, resulting in a more scalable technique with greater versatility for 2D heterostructure assembly³⁷. Exfoliation in water produced a chemically stable suspension of LVO nanoflakes that were collected as a free-standing film via vacuum filtration. In contrast to the LPE in NMP, these nanoflakes exhibited a flat sheet-like morphology that should be compatible with 2D heterostructure assembly. It was also found that vacuum drying this free-standing film at 200 °C reduced the amount of interlayer water that negatively impacts electrochemical performance³⁷.

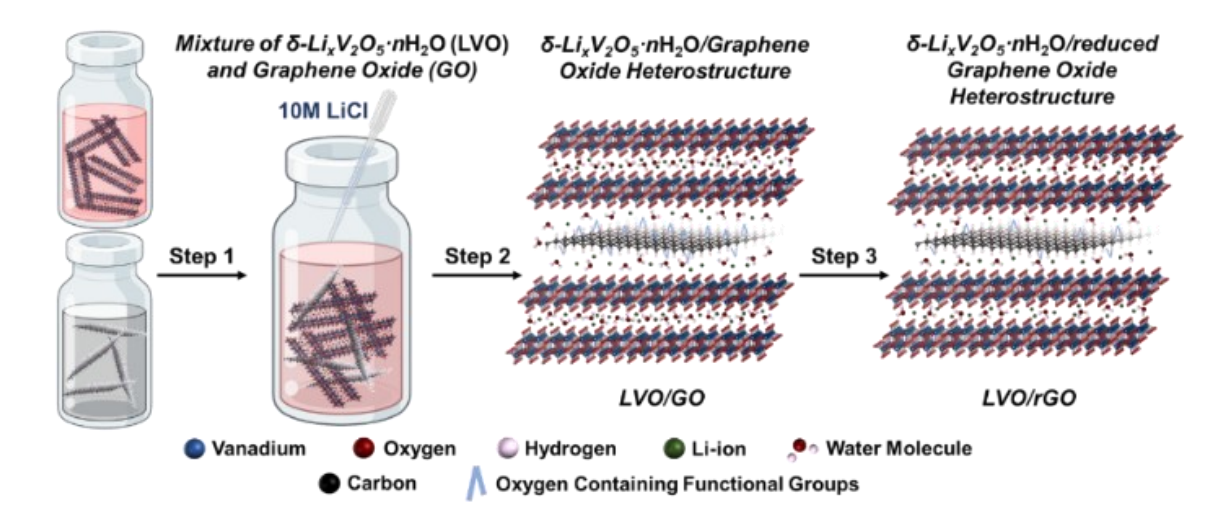


Figure 1. Schematic illustration of the 2D LVO/rGO heterostructure synthesis process developed in this work. Step 1 is the mixing of suspensions containing exfoliated δ -Li_xV₂O₅·nH₂O and single-layer GO nanoflakes followed by Step 2, the slow addition of 10M LiCl to this mixed suspension to form the 2D heterostructure via electrostatic interactions between the negatively charged nanoflakes and positively charged Li-ions. Step 3 is vacuum filtration followed by annealing the heterostructure under vacuum at 200 °C to partially reduce the GO and form the final dehydrated 2D heterostructure³⁸.

This work for the first time utilized a Li-ion driven assembly approach to stack redox active δ -V₂O₅·nH₂O nanoflakes with GO nanoflakes in water to form stabilizing 2D heterointerfaces leading to improved rate capability and capacity retention (**Figure 1**). Thermogravimetric analysis (TGA), Raman spectroscopy, and electron dispersive X-ray spectroscopy (EDX) confirmed the presence of GO and our ability to control the final graphitic content of the heterostructure. TGA and X-ray photoelectron spectroscopy confirmed the reduction of GO after annealing under

vacuum at 200 °C and the partial removal of interlayer water from the LVO phase. Finally, we analyzed the performance of the prepared heterostructures with different LVO/reduced GO (rGO) compositions in Li-ion batteries and found that increasing the fraction of rGO led to improved rate performance and capacity retention, but the charge storage capacity was reduced due to the smaller fraction of the redox active LVO component. We also demonstrate that cation-assembled LVO/rGO electrodes exhibit superior electrochemical performance compared to electrodes prepared through the physical mixing and annealing of LVO and GO nanoflakes. This work shows the prospects of the of cation-driven assembly to stack versatile exfoliated 2D materials and obtain 2D heterostructures with enhanced properties for use in a broad range of technological applications.

2. Experimental Methods

Materials Synthesis

Lithium pre-intercalated bilayered δ -V₂O₅·nH₂O (LVO) was synthesized using a common sol-gel synthesis method^{10, 39}. Briefly, LiCl salt was dissolved in a 15 wt. % hydrogen peroxide solution (Fisher Scientific) to which crystalline α -V₂O₅ (Acros Organics) powder was slowly added, and a red sol formed and precipitated after several hours. The precipitate was aged for four days, washed with DI water using a vacuum filtration apparatus, and dried at 105 °C in air for 24 hours. The dried material was ground into a powder and dried again at 105 °C for 24 hours. The GO was purchased from Graphenea Inc. in a powder form.

Exfoliation and Self Assembly

The LVO powder was exfoliated following a previously developed sonication process using a Qsonica Q125 ultrasonic processor with a 3.175 mm diameter probe tip³⁷. 225 mg of the powder was added to 10 mL of DI water in a 20 mL vial placed in an ice bath. The suspensions were sonicated for 2 hours at an amplitude of 60%, sonication frequency of 20 kHz, and pulse intervals of 6 seconds on and 2 seconds off. After 1 hour of sonication, the ice bath was replaced. The suspension was next centrifuged for 10 mins at 10,000 rpm, and the supernatant was collected for the heterostructure assembly. The concentration was determined by drying 1 mL of suspension in an aluminum boat and weighing the final product after the water evaporated. Separately, the GO powder was dispersed in 40 mL of water and batch sonicated at 60 Hz for 30 mins. The exfoliated LVO suspension (ex-LVO) was added to the GO dispersion with an additional 40 mL of water and stirred for 5 mins. Four different LVO:GO ratios were studied with GO present in 0, 10, 20, and 35 wt. % concentrations. Next, 10 mL of 10 M LiCl solution was dropwise added to the mixed ex-LVO/GO suspension over the course of 8 to 10 minutes to induce the cation-driven assembly and allowed to stir for an additional hour. LiCl salt was chosen so that the ions that induce assembly are the same as the cycling ions in the electrolyte used during electrochemical testing. A color change from deep red to a red orange signaled the initial formation of flocculates after the addition of approximately 2 mL of 10 M LiCl solution (Figure S1 in Supporting Information). The resulting mixture was centrifuged at 6500 RPM to collect the flocculates and remove the concentrated LiCl solution. The flocculates were redispersed in water, washed, and filtered to form a film that was dried at 105 °C. At this stage, the heterostructures are referred to as LVO/GO-0

wt%, LVO/GO-10 wt%, LVO/GO-20 wt%, and LVO/GO-35 wt% depending on the amount of GO nanoflakes used in the cation-driven assembly process. Next, the film was ground into fine powder and annealed at 200 °C under vacuum overnight to obtain rGO and remove excess water³⁷. The final prepared heterostructures are referred to as LVO/rGO-0 wt%, LVO/rGO-10 wt%, LVO/rGO-20 wt%, and LVO/rGO-35 wt%, with rGO indicated that the material was vacuum annealed at 200 °C.

Materials Characterization

The phase composition of the materials during each stage of the synthesis process was determined using a Rigaku benchtop powder X-ray diffraction (XRD) instrument with Cu K_{α} ($\lambda =$ 1.54 Å) radiation. XRD patterns were collected using a step size of 0.02° and step speed of 0.7° 2θ·min⁻¹. Zeta potential measurements were recorded using a Malvern Instruments Zetasizer Nano ZS. The morphology of the particles was captured using a Zeiss Supra 50VP scanning electron microscope (SEM) equipped with Schottky field emission, Everhart-Thornley in-lens secondary electron detector, and dedicated backscatter detector (BSD). In-lens SEM images were acquired using a beam accelerating voltage of 5 kV and 5 mm working distance (WD). Images acquired using the BSD for EDX analysis were captured at a 15 mm WD at 15 kV. Elemental analysis was carried out using an equipped Oxford EDX attachment. Additionally, samples were sputter coated with a thin ~5 nm layer of Pt/Pd to prevent surface charging and improve image quality. For scanning transmission electron microscopy (STEM) characterization, an electron-transparent cross-sectional sample was produced from a vacuum filtrated film by focused ion beam (FIB) liftout. Annular dark-field and bright-field STEM imaging, as well as electron energy-loss spectroscopy (EELS) were then performed on an aberration-corrected Nion UltraSTEM 100 operated at 100 kV with a probe semiconvergence angle of ~31 mrad. Images and EELS maps were acquired with a dose of $\sim 10^4$ e⁻/Å² (images slightly below and EELS maps slightly above), which was sufficiently low to preserve the atomic-scale structure of the materials. Water and GO contents were evaluated using thermogravimetric analysis (TGA) under ambient air flow using a TA Instruments Q50 by evaluating weight loss from room temperature to 1000 °C using a heating rate of 10 °C·min⁻¹. Raman spectra were collected from 100 to 2000 cm⁻¹, using a Renishaw inVia Raman microscope equipped with a 514 nm Ar-ion laser. XPS measurements were recorded on a Physical Electronics VersaProbe 5000 using a monochromatic Al Kα source and charge

compensation. The high-resolution V 2p spectra were taken at a pass energy of 23.5 eV with a step size of 0.05 eV. Peak fitting and data analysis were carried out using CasaXPS software. A Shirley background was used for V 2p spectra quantification.

Electrode and Cell Fabrication

Electrodes were fabricated by first grinding the active material (70 wt. %) and acetylene black (20 wt. %) in a mortar with pestle. Next, this mixture was dispersed in poly(vinylidene fluoride) (10 wt. %) and N-methyl-2-pyrrolidone (NMP) to form a viscous slurry using a Flacktek SpeedMixer. The prepared slurry was cast on aluminum foil and dried in a fume hood under room temperature overnight before being placed in an oven at 105 °C for 12 h. 10 mm electrode disks were punched from the dried films. Coin cells were assembled in an argon filled glovebox. Control films were made by dry physical mixing ex-LVO and GO in 90/10, 80/20, and 65/35 weight ratios by grinding in a mortar with pestle and annealed at 200 °C under vacuum overnight to remove excess water from LVO and reduce GO, similar to heterostructure materials. These samples will be described as 'physically mixed electrodes' in figures and during discussion (e.g., LVO/GO-10 wt% mixed). Electrodes were then fabricated using these materials following the same procedure as described above. Each electrode has an active mass loading between 0.40 and 0.75 mg cm⁻².

Electrochemical Testing

All electrochemical data was collected using 2032 type coin cells. Metallic Li (Alfa Aesar) served as both the counter and reference electrodes, a polypropylene and polyethylene membrane (2325, Celgard USA) served as the separator, and the electrolyte was 1 M LiPF₆ dissolved in a 1:1 (v:v) mixture of ethylene carbonate (EC) and diethyl carbonate (DEC) (Gotion LP40). Cyclic voltammograms (CVs) were collected using a BioLogic VP3 potentiostat at a sweep rate of 0.1 mV s⁻¹. Galvanostatic cycling experiments were run at a 20 mA·g⁻¹ specific current on an Arbin battery testing station. Lastly, rate capability experiments were conducted for 10 cycles each at specific currents of 20 mA g⁻¹, 50 mA g⁻¹, 100 mA g⁻¹, 200 mA g⁻¹, and 20 mA g⁻¹. Finally, electrochemical impedance spectroscopy (EIS) measurements were performed using a Gamry potentiostat by applying an alternating voltage in the frequency range between 10 mHz and 200 kHz at Voc, 0% state-of-charge (SOC), and 100% SOC during the first cycle. EIS measurements were again taken at 0% SOC and 100% SOC after 10 cycles at 20 mA g⁻¹. Here, the SOC was

defined as a range between the upper and lower limits of the voltage window (100% SOC at 4.0 V and 0% SOC at 2.0 V).

3. Results and Discussion

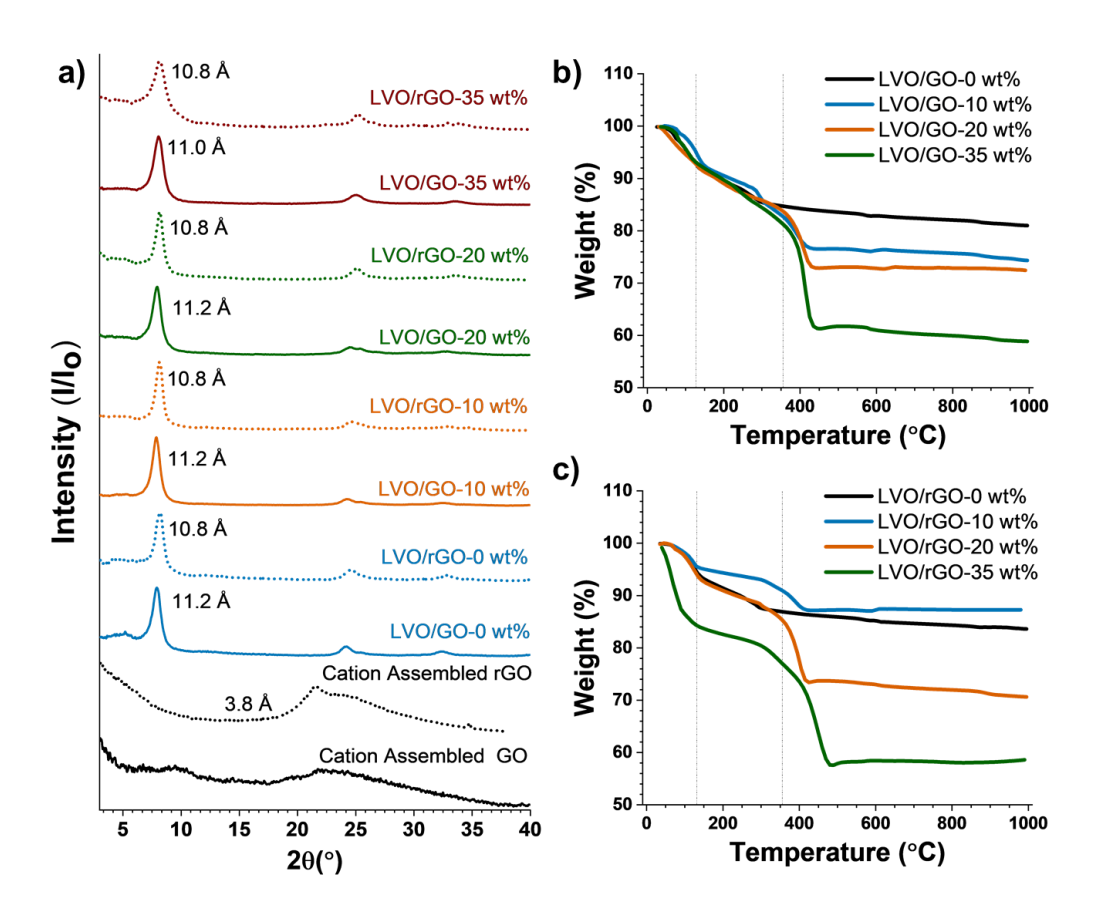


Figure 2. (a) XRD patterns of assembled LVO/(r)GO materials and pure graphene oxide before and after annealing at 200 °C under vacuum. (b,c) TGA weight loss curves of assembled (b) LVO/GO materials before and (c) LVO/rGO materials after annealing at 200 °C under vacuum.

The LVO/rGO heterostructures were synthesized using a cation-driven assembly to draw together negatively charged bilayered vanadium oxide and GO nanoflakes in different ratios via electrostatic interactions induced by Li-ions sourced from LiCl dissociation. The zeta potential curves of ex-LVO nanoflakes, GO nanoflakes, and an ex-LVO/GO-20 wt% nanoflake mixture are shown in **Figure S2** in **Supporting Information**. Each curves shows high magnitude negative potentials of -31, -44, and -41 mV, respectively, which is conducive to this synthesis strategy and consistent with previously reported results^{37, 40}. The annealing at 200 °C under vacuum was used to both reduce the interlayer water content of LVO for better long-term stability³⁷ as well as obtain reduced GO (rGO) to increase its electronic conductivity^{41, 42}. Prior to annealing, each of the assembled heterostructure XRD patterns have the characteristic (00*l*) peaks that are typical of

layered structures (Figure 2a). The (001) peak is located at 7.9-8.0 $^{\circ}$ 20 and corresponds to the dspacing, or the distance between the centers of the vanadium oxide bilayers, of 11.0-11.2 Å. Bragg's law was used to calculate the d-spacing for each sample shown next to the (001) peak in Figure 2a and Figure S3 (Supporting Information). All LVO/GO materials prior to annealing exhibit almost identical XRD patterns without any signal that could be attributed to GO. This result can likely be attributed to the fact that the LVO nanoflakes are not single layer; and therefore, still induce a strong (001) signal. Further, the GO nanoflakes could be irregularly dispersed throughout the heterostructure making their signal in XRD patterns invisible. Additionally, the XRD pattern for GO nanoflakes that were assembled with LiCl also did not show any prominent peaks. In contrast, the XRD pattern for the LVO/rGO-35 wt% mixed material after annealing does show an increase in intensity above 20° 20 that could correspond to agglomerated rGO nanoflakes. This feature does not appear in the LVO/rGO-35 wt% sample prepared by cation-induced assembly likely because the rGO nanoflakes are better dispersed throughout the heterostructure and form an interface predominantly with the vanadium oxide bilayers. The XRD patterns of the heterostructure samples after annealing all feature a (001) peak shift to higher 8.2° 20 values corresponding to lower d-spacings of 10.8 Å. This result indicates a loss of crystallographic water in the LVO structure that occurred during annealing. This premise is further supported in the TGA curves.

The TGA weight loss curves of the cation assembled LVO/GO heterostructures shown in Figure 2b exhibit weight loss regions corresponding to four key components. Weight loss that occurs below 110 °C can be attributed to physiosorbed water. In addition, LVO structural water is lost between 110 °C and 400 °C, and simultaneously, oxygen functional groups on GO are removed between 150 °C and 350 °C (Figure S4 in Supporting Information). The inflection point indicating the loss of oxygen functional groups can be seen at approximately 285 °C for the LVO/GO-10 wt% sample curve. In contrast, the LVO/GO-20 wt% and LVO/GO-35 wt% samples do not exhibit clear weight loss attributed to the loss of oxygen groups. This disparity could potentially be explained by the difference in interactions between GO and LVO as the GO content increases. To estimate the GO content, the weight loss from the structural water in the LVO/GO-0 wt% material was subtracted from the weight loss for each of the assembled heterostructures that occurred above 110 °C. The actual GO content in LVO/GO-10 wt%, LVO/GO-20 wt% and LVO/GO-35 wt% was estimated

to be 11 wt%, 15 wt%, and 29 wt%, respectively. It's possible that the GO content of the LVO/GO-20 wt % and LVO/GO-35 wt% samples were underestimated because they have less structural water compared to the 10 wt% sample, made more plausible by the reduced amount of LVO which holds this water content. Nevertheless, the observed trend agrees with the GO loading in the cation-driven assembly process confirming that no significant loss of GO occurred. After the samples were annealed (Figure 2c), the weight loss that occurred between 110 °C and 350 °C was reduced. This result is due to the removal of LVO structural water and oxygen functional groups, in agreement with previous studies on bilayered vanadium oxide³⁷ and Figure S4 in Supporting Information. The LVO/GO-0 wt% sample experienced 1% greater weight loss than the LVO/rGO-0 wt% sample which agrees with XRD patterns that exhibit peak shifting to higher 20 values due to a lower amount of interlayer water content.

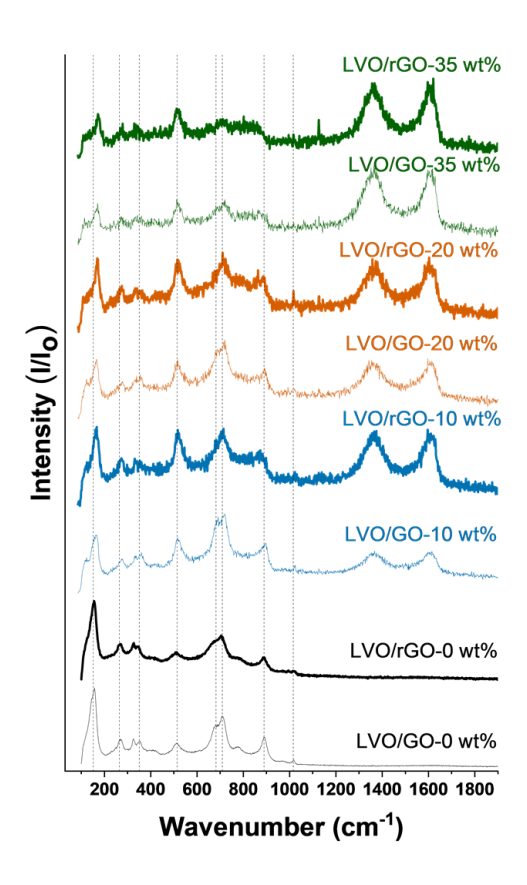


Figure 3. Raman spectra of the of the assembled LVO/(r)GO materials before and after annealing at 200 °C under vacuum.

after vacuum annealing, each of the assembled heterostructures was characterized using Raman spectroscopy (**Figure 3**). The first prominent peak at ~157 cm⁻¹ is present in the Raman spectrum of each material and attributed to the skeletal bending of the bilayered vanadium oxide structure. However, this skeletal bending peak moves to higher wavenumbers of approximately 167 cm⁻¹, 170 cm⁻¹, and 173 cm⁻¹ for the Li-ion assembled LVO/GO nanoflakes with GO content of 10 wt%, 20 wt%, and 35 wt%, respectively. This peak shift could be attributed to interactions between the LVO and (r)GO layers. The remaining characteristic LVO peaks in the fingerprint region up to 1000 cm⁻¹ are denoted by dashed lines. They are fairly consistent between each sample and in agreement with previously reported Raman spectra of bilayered vanadium oxides^{45,46}. The dashed lines at approximately 350 and 685 cm⁻¹ correspond to the bending and stretching of vanadium bonded to the interlayer crystallographic water, respectively. While these peaks can be identified in each of the materials, there is a reduction in intensity of these peaks after annealing at 200 °C for each respective heterostructure. This result indicates a reduction in crystallographic water after annealing^{37,43}, in agreement with both the XRD patterns and TGA weight loss curves.

The second region of interest in the Raman spectra is from 1200 – 1700 cm⁻¹ where the D and G bands of sp² bonded carbon structure occur at about 1370 and 1580 cm⁻¹, respectively. These bands give an indication of how defect rich or graphitic the carbon material is based on their relative intensities (i.e., a higher relative G band is indicative of a sample with more graphitic carbon)^{47, 48}. These peaks are only present in samples that were assembled with GO which further confirms the presence of GO in the heterostructure. In addition, the intensity of the D and G bands increases relative to the fingerprint region of LVO for the samples that were assembled with a higher GO content. However, the D band does not seem to decrease in intensity relative to the G band after annealing at 200°C under vacuum. It's possible that increasing the annealing temperature may increase the G band intensity relative to the D band, but a previous systemic study of GO reduction also did not observe drastic changes in the ratio and instead relied on XPS spectra to show the removal of the oxygen functional groups⁴⁹. In total, the Raman spectra help confirm the TGA results that also indicated that an increase in GO content during the cation-driven LVO/GO assembly process translated to more GO in the final heterostructure.

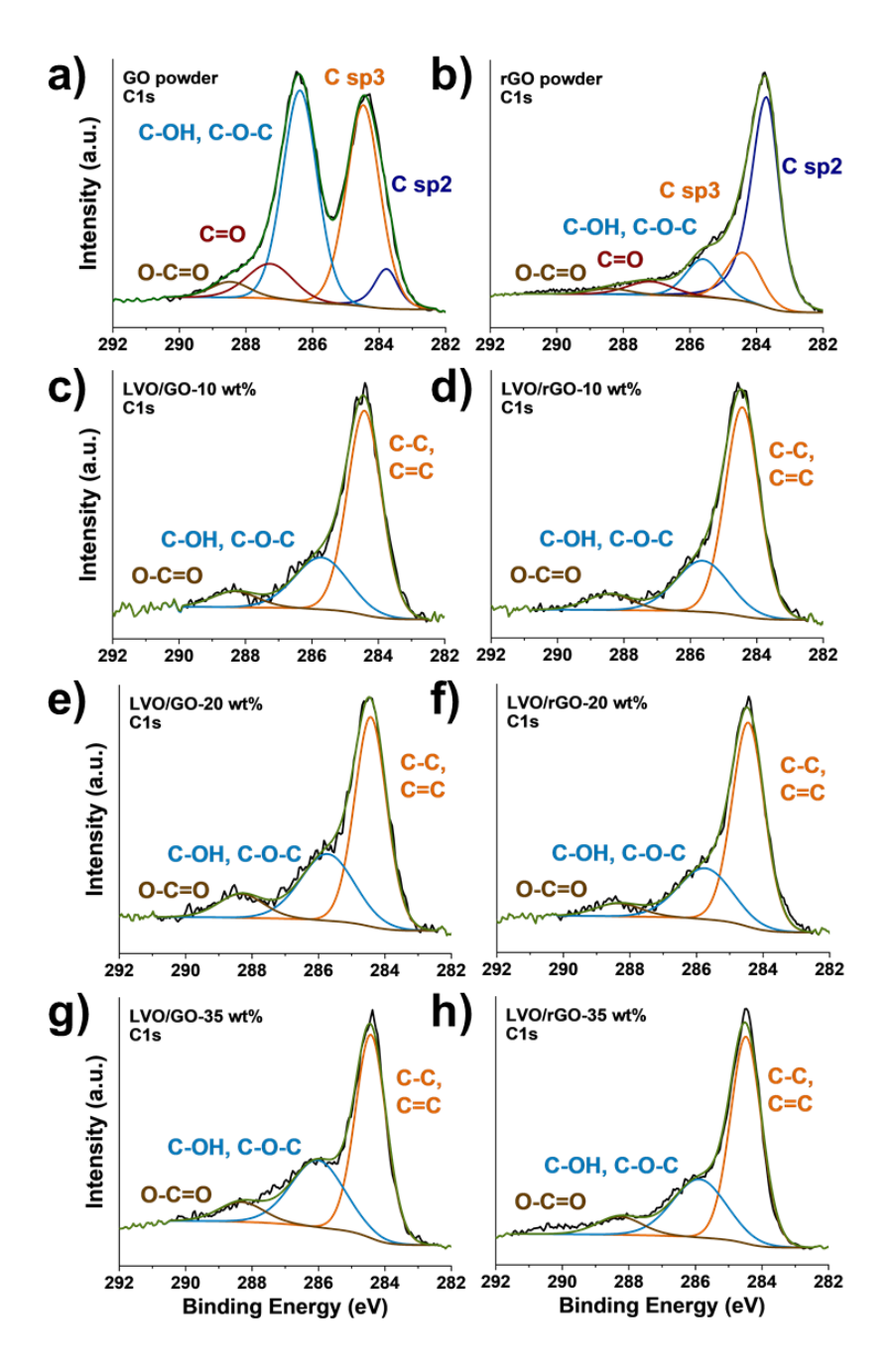


Figure 4. XPS spectra of the C1s region of (a) GO, (b) rGO, (c, e, g) cation-assembled LVO/GO heterostructures before annealing, and (d, f, h) cation-assembled LVO/rGO heterostructures after annealing at 200 °C under vacuum

XPS was used to gain a better understanding of the effect of annealing at 200 °C on both the GO layers and the oxidation state of vanadium in LVO. The spectra of the C1s and V2p regions for GO and each heterostructure are displayed in **Figure 4** and **Figure S5** (**Supporting**

Information), respectively, and a summary of the contributions of carbon functional groups and vanadium oxidations states are shown in Table S1 and Table S2 (Supporting Information). As mentioned, the reduction of GO can be seen more clearly in XPS spectra compared to Raman spectroscopy. Before annealing, the GO spectrum (Figure 4a) shows approximately 6% sp² hybridized carbon. Whereas after annealing, sp² hybridized carbon exhibits the strongest signal in the rGO spectrum at 63%, followed by sp³ hybridized carbon at 16%, C-O single bonds at 13%, C=O double bonds at 6%, and O-C=O functional groups at C=O double bonds at 2% consistent with previously reported results (Figure 4b)⁵⁰. This outcome confirms that annealing at 200 °C under vacuum was sufficient to significantly reduce GO and improve its electronic conductivity⁴¹, ⁴². In comparison, the C1s region is much harder to interpret for the LVO/GO heterostructure spectra (Figure 4, c-h) due to a weaker C signal caused by the high vanadium oxide content as well as larger relative signal from adventitious carbon. Due to these factors, the C sp² signal could not be deconvoluted from the C sp³ signal. However, there is a consistent increase in the area corresponding to C-C and C=C bonding and a reduction in the XPS signal from C and O bonds in each respective heterostructure XPS spectra after annealing. These trends suggest that the GO present in the heterostructures was reduced by annealing at 200 °C under vacuum.

Analysis of the V2p region shows that vanadium exists in a mixed V⁵⁺ and V⁴⁺ oxidation state in each LVO/(r)GO heterostructure sample before and after annealing (**Figure S5** in **Supporting Information**). The samples prepared with 10, 20, and 35 wt.% GO before vacuum annealing have average oxidation states of 4.96, 4.94, and 4.93, respectively (**Figure S5a, c** and **e, Supporting Information**). This slight reduction could be attributed to Li-ions intercalated into the interlayer region of LVO^{10 46}. After annealing, XPS spectra of the samples prepared with 10, 20, and 35 wt.% GO show average vanadium oxidation states of 4.93, 4.89, and 4.85, respectively (**Figure S5b, d,** and **f, Supporting Information**). The secondary reduction after annealing is most likely due to the formation of oxygen vacancies, a common defect that occurs when treating LVO at elevated temperatures^{37, 51, 52}. The XPS spectra of the C1s and V2p regions of the (r)GO and LVO/(r)GO heterostructures confirm that there are interactions between LVO and (r)GO layers as well as that GO was reduced to rGO through vacuum annealing at 200 °C.

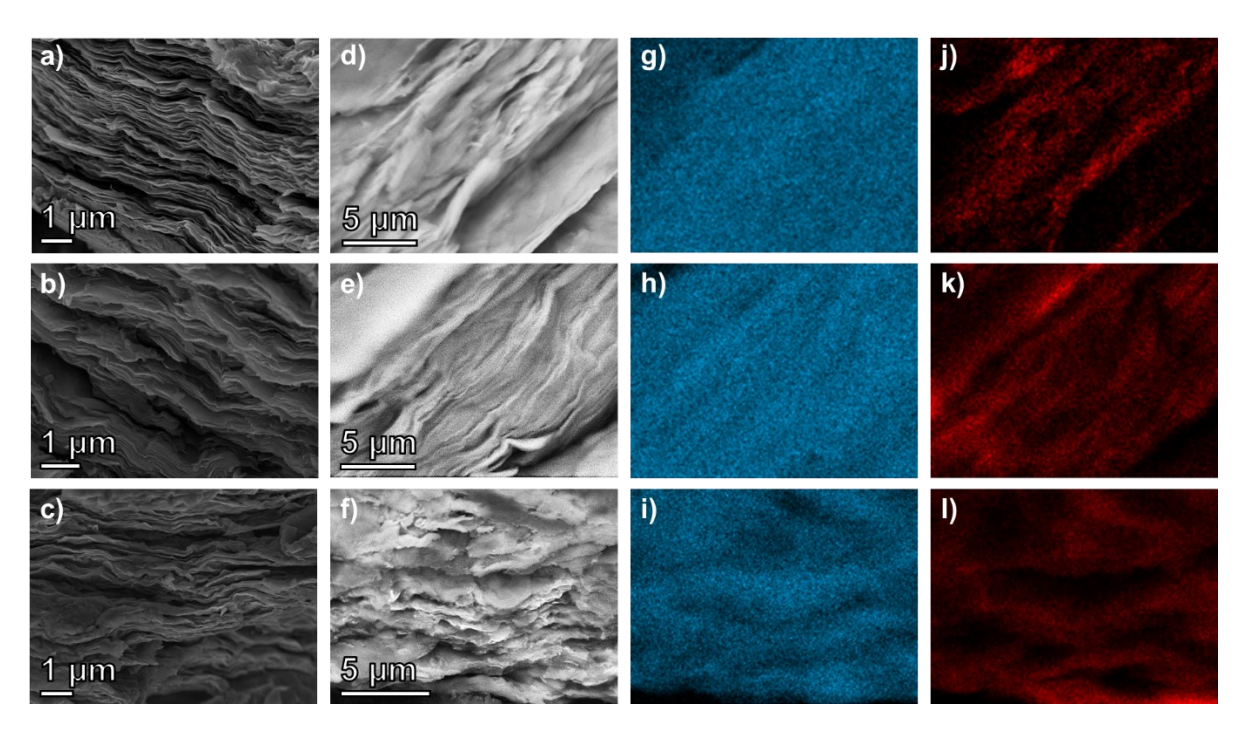


Figure 5. Cross-sectional SEM images of the LVO/GO-10 wt%, LVO/GO-20 wt%, and LVO/GO-35 wt% heterostructures, respectively taken with an (a-c) in-lens detector, (d-f) BSD, and the (g-i) vanadium signal and (j-l) carbon signal captured using EDX simultaneously acquired with the BSD images.

Cross-sectional SEM images of LVO/GO heterostructures were analyzed to understand how chemically dissimilar nanoflakes were stacked during cation-driven assembly. A BSD was used in conjunction with EDX to help determine the composition of the heterostructures as well as the distribution of specific elements, all shown in **Figure 5**. The LVO/GO-10, 20 and 35 wt.% materials each exhibit nanoflakes stacked together to form a 2D interface (**Figure 5**, **a-c**). The cross-sectional BSD images (**Figure 5**, **d-f**) exhibit darker and lighter regions that generally correspond to lighter and heavier elements, respectively. The EDX elemental maps of vanadium (**Figure 5**, **g-i**) and carbon (**Figure 5**, **j-l**) were used in conjunction with the BSD images to identify LVO and GO nanoflake regions in the heterostructures. The maps show heterointerface formation between LVO and GO on the micron scale which is likely due to some agglomeration of chemically identical nanoflakes. However, this technique is not able to analyze the interface of individual LVO/GO nanoflakes due to the limitations of SEM imaging resolution. Most importantly, the signal from these two elements do show a layered distribution helping confirm that cation-driven assembly formed a 2D heterointerface between GO and LVO. Moreover, the

vanadium to carbon signal ratio decreases as the weight percentage of GO increases. EDX spectra of the LVO/GO-10 wt.%, 20 wt.%, and 35 wt.% samples collected V/C molar ratios of approximately 7.5, 2.4, and 1.4, respectively, trends in agreement with TGA results (**Figure S6** and **Table S3** in **Supporting Information**).

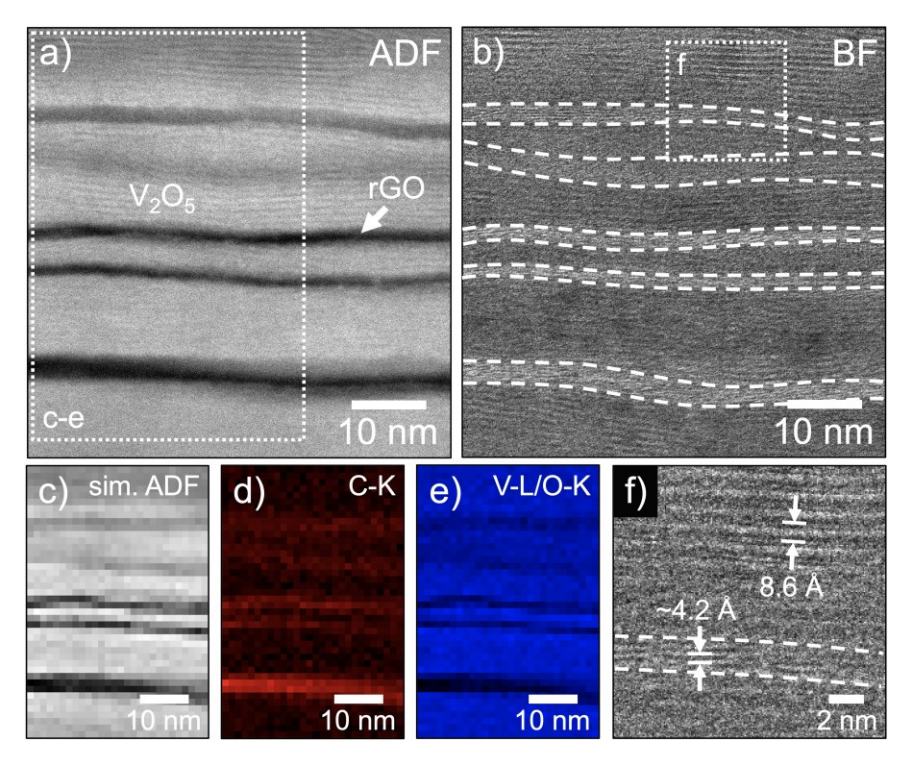


Figure 6. High-resolution STEM and EELS characterization of LVO/rGO-20 wt% 2D heterostructure. (a) ADF-STEM image of nanometer-scale rGO sheets between thin LVO layers. Dashed box indicates approximate region where EELS in (c-e) was acquired. (b) BF-STEM image simultaneously acquired with (a), showing atomic-scale structure of the LVO and rGO layers. Dashed lines highlight rGO sheet locations and the dashed box indicates the zoomed region shown in (f). (c-e) EELS mapping of region indicated in (a), with simultaneous ADF-STEM image, integrated C K-edge, and integrated V L-/O K-edges displayed, respectively. (f) Zoomed region from (b) showing interlayer spacings of 8.6 Å and ~4.2 Å for LVO and rGO, respectively.

To explore individual LVO/GO nanoflake heterostructures at higher resolution, scanning transmission electron microscopy (STEM) and electron energy-loss spectroscopy (EELS) were performed on a cross-sectional LVO/rGO-20 wt% sample produced by focused ion beam (**Figure 6**). As displayed in **Figure 6a**, annular dark-field (ADF) STEM imaging clearly shows the presence of heterostructures consisting of rGO sheets with thicknesses down to the nanometer scale between layers of LVO. Bright-field (BF) STEM imaging, as shown in **Figure 6b**, more clearly reveals the atomic-scale structure of these materials, both of which are layered in the

stacking direction. EELS mapping (**Figure 6c-e**) further confirms that the light and dark layers in the ADF-STEM images are composed primarily of vanadium/oxygen and carbon, respectively. A zoomed region of the BF-STEM image (**Figure 6f**) shows that the local interlayer spacings of the LVO and rGO layers are 8.6 Å and ~4.2 Å (with a broader distribution of rGO spacings), respectively. The reduced interlayer distance in LVO as compared to XRD measurements can be attributed to the local (STEM) and bulk (XRD) nature of the measurements, as well as the film processing conditions required for the preparation of the sample for imaging.³⁷ Further ADF- and BF-STEM images of heterostructures can be found in **Figure S7** in **Supporting Information**.

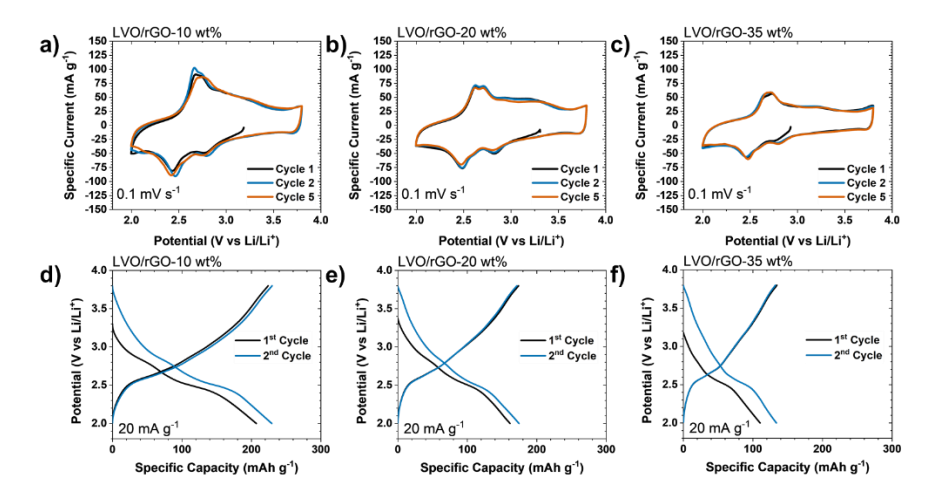


Figure 7. (a-c) CV and (d-f) galvanostatic discharge/charge curves of Li-ion cells containing (a, d) LVO/rGO-10 wt%, (b, e) LVO/rGO-20 wt%, and (c, f) LVO/rGO-35 wt% electrodes. The color-coded cycles are shown as a legend within each figure panel.

Figure 7 shows the CV and galvanostatic discharge/charge (GDC) curves exhibited by the LVO/rGO heterostructure electrodes in Li-ion half-cells. The CV curves of each heterostructure (**Figure 7**, **a-c**) exhibit a broad cathodic peak at 2.8 V, a more prominent cathodic peak at 2.45 V, and a corresponding doublet anodic peak at approximately 2.7 V vs Li/Li⁺. This shape is consistent with BVO materials synthesized previously and is indicative of highly reversible ion intercalation-type behavior ^{16, 37, 46}. This result also confirms that the redox activity of LVO was maintained throughout the processing steps of exfoliation, cation-driven assembly, and vacuum annealing. However, the specific capacity of the CV curves noticeably decrease as the amount of GO increases which signifies that decreasing the relative LVO content limits the total capacity of the electrode. The heterostructure GDC curves for the first and second cycles exhibit plateaus that

agree well with the cathodic and anodic peaks in the CV curves (Figure 7, d-f). The LVO/rGO-10 wt%, LVO/rGO-20 wt%, and LVO/rGO-35 wt% materials show capacities of 200, 161, and 110 mAh g⁻¹ on the first discharge cycle, respectively, a trend in agreement with increasing rGO content. This result confirms that increasing the amount of GO during cation-driven assembly reduces the charge storage capacity of the heterostructure due to the reduced amount of redox active LVO component and absence of the rGO redox activity in the potential window selected for cycling. Interestingly, the capacities of the LVO/rGO-10 wt%, LVO/rGO-20 wt%, and LVO/rGO-35 wt% electrodes on the second discharge are notably higher at 216, 174, and 132 mAh g⁻¹, respectively. This phenomenon could be related to the incorporation of Li-ions between the nanoflakes forming heterostructures during the cation-induced assembly process. Subsequently, these ions were at least partially extracted during the first charge, thereby opening additional sites in the interlayer region for Li-ion intercalation during later discharge cycles. This idea is supported by the initial cycles of the physically mixed reference electrodes shown in Figure S8, a-c (Supporting Information) where the values of the first and second discharge cycle capacities have little discrepancy compared to the LVO/rGO heterostructures prepared via cation-driven assembly.

Each of the heterostructures was cycled at a specific current of 20 mA g⁻¹ for 100 cycles to assess their electrochemical stability (**Figure 8, a-c**). After 100 cycles, the LVO/rGO-10 wt% material demonstrated a specific discharge capacity of 99 mAh g⁻¹, a capacity retention of 46%, and the LVO/rGO-20 wt% electrode showed a 139 mAh g⁻¹ specific discharge capacity and 80% capacity retention. In contrast, the LVO/rGO-35 wt% electrode demonstrated a 127 mAh g⁻¹ specific discharge capacity and 96% capacity retention after 100 cycles. Moreover, the electrode prepared by LVO nanoflake assembly without GO retained only 2% of its second cycle specific discharge capacity after 100 cycles (**Figure S9** in **Supporting Information**) showing the importance of rGO presence in a heterostructure for stable electrochemical cycling. This data shows that increasing the GO content during cation-driven assembly helps stabilize the electrochemical performance of the heterostructures. Interestingly, the capacities of the LVO-enriched 2D heterostructure electrodes with high initial capacities drop below the values demonstrated by the LVO/rGO-20 wt% and LVO/rGO-35 wt% electrodes after 100 cycles. This result indicates a stabilization effect enabled by the heterointerface formation. A similar phenomenon for BVO was observed in the case of oxide/carbon heterointerfaces created via

carbonization of chemically preintercalated dopamine molecules¹⁵ and nanocomposites with graphene and carbon nanotubes¹⁶. It's possible that the rGO in these materials is stabilizing the electrodes by inhibiting the dissolution of LVO in electrolyte, an occurrence observed in previous studies⁵³⁻⁵⁵. In the case of the 2D LVO/rGO heterostructures prepared in this work, the stabilization effect could be attributed to both the formation of bonds between the LVO and rGO surfaces via the Li-ions incorporated between the layers as well as encapsulation of the oxide nanoflakes by rGO nanoflakes preventing active dissolution of LVO in the electrolyte, similar to reported MoO₃/MXene composite electrodes⁵⁶. This encapsulation could also explain why the capacity of the LVO/rGO-35 wt% electrode initially increases. The increased rGO content may initially block electrolyte access to the LVO component, and electrochemical cycling could activate this material by opening diffusion pathways. We do not observe this trend at lower ratios because the reduced rGO content allows the electrolyte to readily interact with LVO.

The performance of the LVO/rGO heterostructure electrodes was also tested at high specific currents, and their respective drops in specific capacity were evaluated to understand their tolerance for fast charging and discharging (Figure 8, d-f). After applying the highest specific current, the discharge/charge rate was brought back to the lowest value to further assess each electrode's stability and recovery. The LVO/rGO-35 wt.% and LVO/rGO-20 wt.% heterostructures retained 75% (110 mAh g⁻¹) and 67% (120 mAh g⁻¹) of their initial capacities after increasing the specific current from 20 mA g⁻¹ to 200 mA g⁻¹, while the LVO/rGO-10 wt% sample retained only 48% (107 mAh g⁻¹) of its initial capacity under the same cycling conditions. More importantly, each of the heterostructures performed significantly better at increased current rates compared to the physically mixed reference electrodes, the rate capability data of which are shown in Figure S8 in Supporting Information. The comparison of 2D heterostructure and physically mixed electrodes illustrates the important role of Li-ions for the heterointerface formation via this top-down fabrication method. Analysis of electrochemical performance shows that cation-driven assembly with Li-ions helps induce and stabilize the formation of stacked 2D layers of GO and exfoliated LVO nanoflakes to mitigate charge storage degradation when applying high specific currents and during extended cycling. The LVO/rGO-35 wt% electrode fully recovered its original capacity after the discharge/charge rate was reduced from 200 mA g⁻¹ to 20 mA g⁻¹, demonstrating the improved electrochemical stability of this heterostructure at high specific currents. In comparison, the LVO/rGO-10 wt.% and LVO/rGO-20 wt.% electrodes recovered ~75% and ~84%

of their initial capacities, respectively. The enhanced rate capability behavior is attributed to the improved electronic conductivity of the LVO/rGO heterostructures enriched with the rGO component providing conductive pathways for electron transport. In total, the LVO/rGO-20 wt % heterostructure exhibits the most promising combination of electrochemical stability and storage capacity. However, we believe that this synthesis method could be improved further by more efficiently exfoliating LVO to acquire thinner nanoflakes and potentially enhance the LVO/rGO interface.

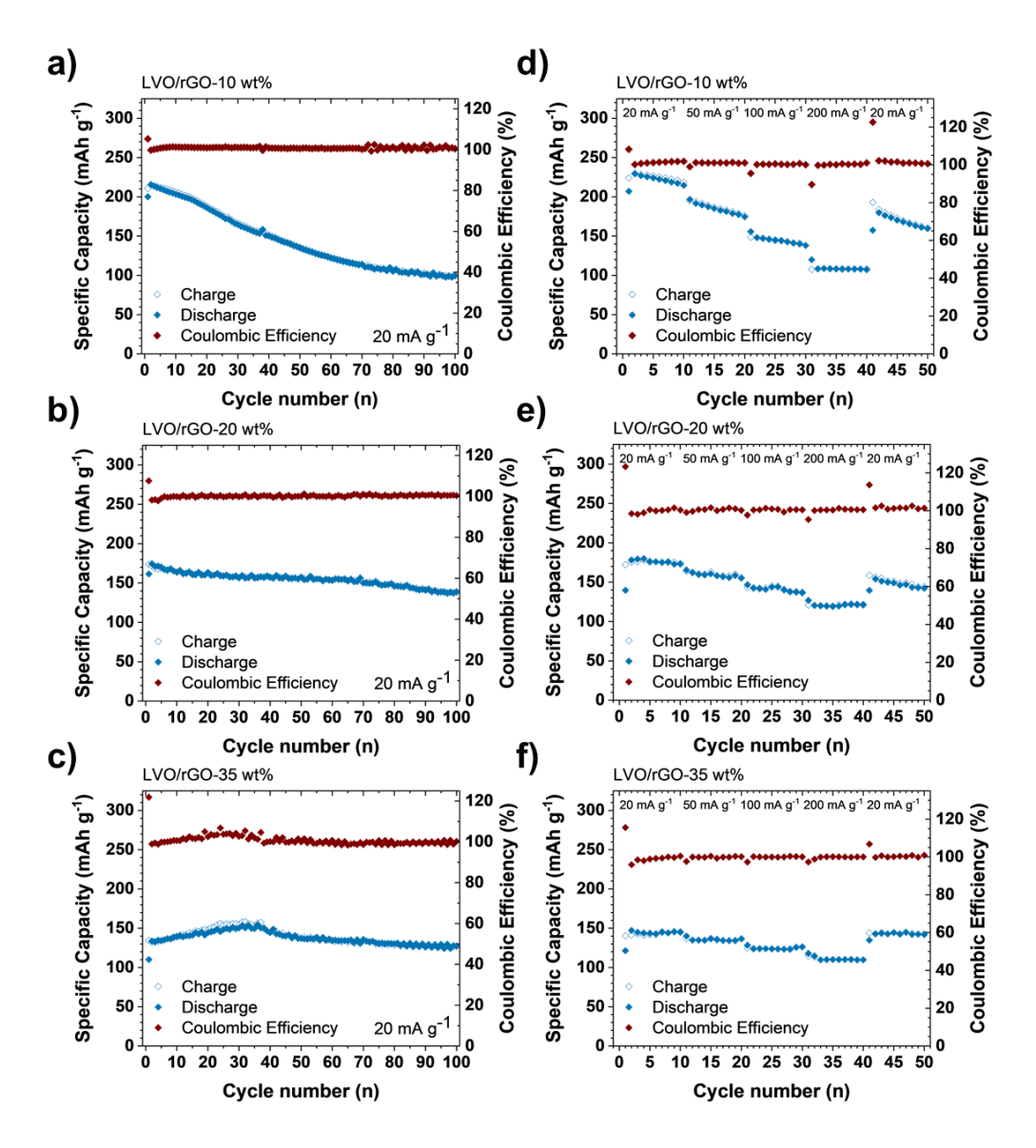


Figure 8. (a-c) Galvanostatic life cycle testing and (d-f) rate capability data of the Li-ion cells containing (a, d) LVO/rGO-10 wt%, (b, e) LVO/rGO-20 wt%, and (c, f) LVO/rGO-35 wt% electrodes.

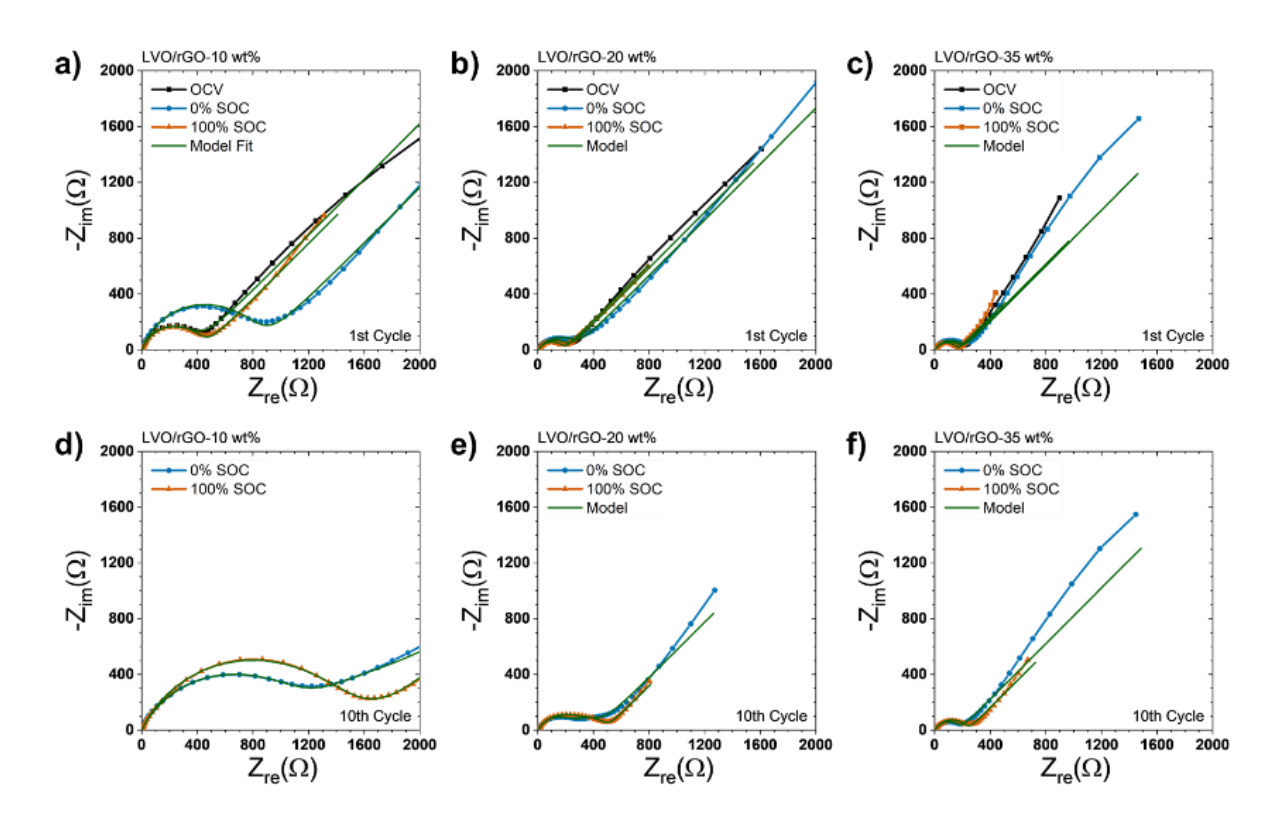


Figure 9. Experimentally obtained Nyquist plots (scattered symbols) of (a) LVO/rGO-10 wt%, (b) LVO/rGO-20 wt%, and (c) LVO/rGO-35 wt% electrodes during the 1st discharge/charge cycle and (d-f) during the 10th discharge/charge cycle. The green solid line corresponds to the Nyquist plots fitting obtained using the equivalent circuit models shown in **Figure S9** (**Supporting Information**).

To evaluate the charge transfer resistance and validate the improved electronic conductivity, EIS measurements for the Li-ion cells containing LVO/rGO heterostructure electrodes were recorded before and after ten discharge/charge cycles. The corresponding Nyquist plots are shown in **Figure 9**. Schematic representations of the proposed equivalent circuits are shown in **Figure S10** in **Supporting Information** and based on previous studies involving vanadium oxide phases with and without the formation of an SEI layer^{14, 57, 58}. R₀ is the non-active component of the resistivity, including the electrolyte resistance, R_{ct} is the charge transfer resistance between the electrode and the electrolyte, CPE_{ct} is the double layer capacitance on the electrode surface, CPE_i and R_i are the capacitance and resistance of the SEI layer that has been modeled in previous work^{14, 59}, and *W* is the Warburg diffusion impedance into the bulk electrode. The model fit parameters are shown in **Table S4** (**Supporting Information**) for each material's EIS measurement at five stages of cycling: OCV, 0% state of charge (SOC) on 1st discharge, 100%

SOC on 1st charge, 0% SOC on 10th discharge, and 100% SOC on 10th charge. During the first cycle (**Figure 9, a-c**) the R_{ct} values decrease as the amount of rGO in the heterostructure increases, probably due to the improved electron transport in the carbon enriched heterostructures. However, after 10 cycles the charge transfer resistance increases notably for the LVO/rGO-10 wt% and LVO/rGO-20 wt% heterostructures as compared to the corresponding values on the first cycle (**Table S4** in **Supporting Information**) which could be indicative of SEI formation, shown as a separate element in the equivalent circuit (**Figure S10b** in **Supporting Information**). Interestingly, the Nyquist plots exhibited by the cells containing LVO/rGO-35 wt% electrode after 10 cycles do not exhibit a significant change in R_{ct} values, and the fit is better using the equivalent circuit that does not have a component corresponding to the SEI layer (**Figure S10a** in **Supporting Information**). This result suggests that the SEI formation on LVO could be suppressed by an rGO encapsulation effect. These trends agree with our finding that increasing the GO content during cation-driven assembly, and thereby increasing the fraction of the LVO/rGO heterointerface, improves electron transport, stabilizes LVO structure and prevents the dissolution of the heterostructure in electrolyte during cycling.

4. Conclusions

For the first time, this work used a top-down cation-driven assembly in water to synthesize stacked 2D heterostructures of LVO and rGO nanoflakes followed by vacuum filtration and annealing. We showed that annealing at 200 °C under vacuum removed excess water stemming from the aqueous-based synthesis method and reduced graphene oxide to form rGO with increased electronic conductivity. The electrochemical cycling results of the LVO/rGO heterostructures prepared with 10, 20, and 35 wt% GO compared to the physically mixed electrodes prepared with the same LVO:GO ratios suggest that Li-ion driven assembly favored the heterointerface formation. The superior electrochemical stability of the 2D heterostructures was attributed to improved structural stability, originating from bonds formed between rGO and LVO nanoflakes that preserved lamellar order of the layers in the LVO structure, and rGO encapsulation effect preventing significant dissolution of LVO nanoflakes in the electrolyte. While increasing the fraction of rGO improves the stability and rate capability of the 2D LVO/rGO heterostructure electrodes, the capacity values scale down according to the decrease in LVO content. The improved electron transport of the heterostructures with enhanced rGO content was supported by

both the rate capability study and decreased charge transfer resistance evidenced by the EIS characterization. However, the optimal ratio between LVO and rGO must be found in order to achieve the best combination of electrochemical stability and capacity. The results of this study suggest the LVO/rGO-20 wt% heterostructure displays the most promising electrochemical performance when accounting for both long-term stability and total storage capacity, but we also support future work dedicated towards more efficient exfoliation of LVO to thinner layers to better disperse conductive phases throughout the assembled structure which could impact the optimal LVO/rGO ratio. This method can also be expanded to incorporate additional exfoliated phases such as other transition metal oxides, transition metal dichalcogenides, and MXenes.

Supporting Information

Images of the LVO/GO heterostructures in solution after cation-driven assembly, zeta potential curves of GO, ex-LVO, and a ex-LVO/GO-20 wt% mixture dispersed in water, XRD patterns of GO powder, rGO powder, and mixed LVO/(r)GO materials, TGA curves of GO and rGO powder, XPS spectra of the V2p region of the cation-assembled LVO/(r)GO heterostructures and Tables summarizing the binding energies and at% of each of their respective functional groups, top-down SEM images, EDX maps, and STEM images of the LVO/GO heterostructures and a summary table of the results, rate capability GDC curves and rate capability data of each of the physically mixed electrodes, life cycle data of the LVO/rGO-0 wt% electrode, equivalent circuit models used fit the experimentally obtained Nyquist plots and a summary table of the circuit fitting parameters

Acknowledgements

This work was supported by the National Science Foundation (NSF) under Grant No. DMR-1752623. We thank Drexel's Materials Characterization Core (MCC) facility for providing access to characterization instruments. STEM and EELS research were supported by the Center for Nanophase Materials Sciences (CNMS), which is a US Department of Energy, Office of Science User Facility at Oak Ridge National Laboratory.

References

- (1) Huang, S.-Z.; Cai, Y.; Jin, J.; Li, Y.; Zheng, X.-F.; Wang, H.-E.; Wu, M.; Chen, L.-H.; Su, B.-L. Annealed Vanadium Oxide Nanowires and Nanotubes as High Performance Cathode Materials for Lithium Ion Batteries. *Journal of Materials Chemistry A* **2014**, *2* (34), 14099. DOI: 10.1039/c4ta02339k.
- (2) Wang, H.-E.; Chen, D.-S.; Cai, Y.; Zhang, R.-L.; Xu, J.-M.; Deng, Z.; Zheng, X.-F.; Li, Y.; Bello, I.; Su, B.-L. Facile Synthesis of Hierarchical and Porous V₂O₅ Microspheres as Cathode Materials for Lithium Ion Batteries. *Journal of Colloid and Interface Science* **2014**, *418*, 74-80.
- (3) Pan, A.; Zhang, J.-G.; Nie, Z.; Cao, G.; Arey, B. W.; Li, G.; Liang, S.-Q.; Liu, J. Facile Synthesized Nanorod Structured Vanadium Pentoxide for High-Rate Lithium Batteries. *Journal of Materials Chemistry* **2010**, *20* (41), 9193. DOI: 10.1039/c0jm01306d.
- (4) Chernova, N. A.; Roppolo, M.; Dillon, A. C.; Whittingham, M. S. Layered Vanadium and Molybdenum Oxides: Batteries and Electrochromics. *Journal of Materials Chemistry* **2009**, *19* (17), 2526. DOI: 10.1039/b819629j.
- (5) Bai, H.; Liu, Z.; Sun, D. D.; Chan, S. H. Hierarchical 3D Micro-/Nano-V₂O₅ (Vanadium Pentoxide) Spheres as Cathode Materials for High-Energy and High-Power Lithium Ion-Batteries. **2014**, *76*, 607-613. DOI: 10.1016/j.energy.2014.08.058.
- (6) Zhang, X.; Hou, L.; Ciesielski, A.; Samorì, P. 2D Materials Beyond Graphene for High-Performance Energy Storage Applications. *Advanced Energy Materials* **2016**, *6* (23), 1600671. DOI: 10.1002/aenm.201600671.
- (7) Chen, W.; Zhang, R.; Sun, Y.; Wang, J.; Fan, Y.; Liu, B. Preparation, Properties, and Electronic Applications of 2D Bi₂O₂Se. *Advanced Powder Materials* **2022**, 100080.
- (8) Pomerantseva, E.; Gogotsi, Y. Two-Dimensional Heterostructures for Energy Storage. *Nature Energy* **2017**, *2* (7), 17089.
- (9) Petkov, V.; Trikalitis, P. N.; Bozin, E. S.; Billinge, S. J. L.; Vogt, T.; Kanatzidis, M. G. Structure of V₂O₅·nH2O Xerogel Solved by the Atomic Pair Distribution Function Technique. *Journal of the American Chemical Society* **2002**, *124* (34), 10157-10162. DOI: 10.1021/ja026143y.
- (10) Clites, M.; Pomerantseva, E. Bilayered Vanadium Oxides by Chemical Pre-Intercalation of Alkali and Alkali-Earth Ions as Battery Electrodes. *Energy Storage Materials* **2018**, *11*, 30-37. DOI: 10.1016/j.ensm.2017.09.005.
- (11) Pomerantseva, E. Chemical Preintercalation Synthesis of Versatile Electrode Materials for Electrochemical Energy Storage. *Accounts of Chemical Research* **2023**, *56* (1), 13-24. DOI: 10.1021/acs.accounts.2c00193.
- (12) Huang, X.; Qi, X.; Boey, F.; Zhang, H. Graphene-Based Composites. *Chem. Soc. Rev.* **2012**, *41* (2), 666-686. DOI: 10.1039/c1cs15078b.
- (13) Moretti, A.; Giuli, G.; Trapananti, A.; Passerini, S. Electrochemical and Structural Investigation of Transition Metal Doped V₂O₅ Sono-Aerogel Cathodes for Lithium Metal Batteries. *Solid State Ionics* **2018**, *319*, 46-52.
- (14) Liu, Q.; Li, Z.-F.; Liu, Y.; Zhang, H.; Ren, Y.; Sun, C.-J.; Lu, W.; Zhou, Y.; Stanciu, L.; Stach, E. A.; et al. Graphene-Modified Nanostructured Vanadium Pentoxide Hybrids with Extraordinary Electrochemical Performance for Li-ion Batteries. **2015**, *6*, 6127. DOI: 10.1038/ncomms7127.
- (15) Clites, M.; Andris, R.; Cullen, D. A.; More, K. L.; Pomerantseva, E. Improving Electronic Conductivity of Layered Oxides through the Formation of Two-Dimensional Heterointerface for Intercalation Batteries. *ACS Applied Energy Materials* **2020**. DOI: 10.1021/acsaem.0c00274.

- (16) Averianov, T.; Pomerantseva, E. Composite Li-ion Battery Cathodes Formed via Integration of Carbon Nanotubes or Graphene Nanoplatelets into Chemical Preintercalation Synthesis of Bilayered Vanadium Oxides. *Journal of Alloys and Compounds* **2022**, *903*, 163929.
- (17) Andris, R.; Averianov, T.; Pomerantseva, E. Phase Transformation and Electrochemical Charge Storage Properties of Vanadium Oxide/Carbon Composite Electrodes Synthesized via Integration with Dopamine. *Journal of the American Ceramic Society* **2022**. DOI: 10.1111/jace.18502.
- (18) Liu, S.; Yin, Y.; Hui, K. S.; Hui, K. N.; Lee, S. C.; Jun, S. C. High-Performance Flexible Quasi-Solid-State Supercapacitors Realized by Molybdenum Dioxide@Nitrogen-Doped Carbon and Copper Cobalt Sulfide Tubular Nanostructures. *Advanced Science* **2018**, *5* (10), 1800733. DOI: 10.1002/advs.201800733.
- (19) Liu, S.; Yin, Y.; Shen, Y.; Hui, K. S.; Chun, Y. T.; Kim, J. M.; Hui, K. N.; Zhang, L.; Jun, S. C. Phosphorus Regulated Cobalt Oxide@Nitrogen-Doped Carbon Nanowires for Flexible Quasi-Solid-State Supercapacitors. *Small* **2020**, *16* (4), 1906458. DOI: 10.1002/smll.201906458.
- (20) Yan, J.; Ren, C. E.; Maleski, K.; Hatter, C. B.; Anasori, B.; Urbankowski, P.; Sarycheva, A.; Gogotsi, Y. Flexible MXene/Graphene Films for Ultrafast Supercapacitors with Outstanding Volumetric Capacitance. *Advanced Functional Materials* **2017**, *27* (30), 1701264. DOI: 10.1002/adfm.201701264.
- (21) Xiong, P.; Ma, R.; Sakai, N.; Sasaki, T. Genuine Unilamellar Metal Oxide Nanosheets Confined in a Superlattice-like Structure for Superior Energy Storage. *ACS Nano* **2018**, *12* (2), 1768-1777. DOI: 10.1021/acsnano.7b08522.
- (22) Tian, W.; Vahidmohammadi, A.; Wang, Z.; Ouyang, L.; Beidaghi, M.; Hamedi, M. M. Layerby-Layer Self-Assembly of Pillared Two-Dimensional Multilayers. *Nature Communications* **2019**, *10* (1). DOI: 10.1038/s41467-019-10631-0.
- (23) Jiang, J.-M.; Li, Z.-W.; Zhang, Z.-T.; Wang, S.-J.; Xu, H.; Zheng, X.-R.; Chen, Y.-X.; Ju, Z.-C.; Dou, H.; Zhang, X.-G. Recent Advances and Perspectives on Prelithiation Strategies for Lithium-Ion Capacitors. *Rare Metals* **2022**, *41* (10), 3322-3335. DOI: 10.1007/s12598-022-02050-w.
- (24) Heising, J.; Kanatzidis, M. G. Exfoliated and Restacked MoS₂ and WS₂: Ionic or Neutral Species? Encapsulation and Ordering of Hard Electropositive Cations. *Journal of the American Chemical Society* **1999**, *121* (50), 11720-11732. DOI: 10.1021/ja991644d.
- (25) Miremadi, B. K.; Morrison, S. R. Preparation of Alternating MoS₂ and WS₂ Single Layers to Form a New MoWS₄ Structure. *Journal of Applied Physics* **1990**, 67 (3), 1515-1520. DOI: 10.1063/1.345661.
- (26) Zhao, D.; Clites, M.; Ying, G.; Kota, S.; Wang, J.; Natu, V.; Wang, X.; Pomerantseva, E.; Cao, M.; Barsoum, M. W. Alkali-Induced Crumpling of Ti₃C₂T_x (MXene) to Form 3D Porous Networks for Sodium Ion Storage. *Chemical Communications* **2018**, *54* (36), 4533-4536. DOI: 10.1039/c8cc00649k.
- (27) Vahidmohammadi, A.; Mojtabavi, M.; Caffrey, N. M.; Wanunu, M.; Beidaghi, M. Assembling 2D MXenes into Highly Stable Pseudocapacitive Electrodes with High Power and Energy Densities. *Advanced Materials* **2019**, *31* (8), 1806931. DOI: 10.1002/adma.201806931.
- (28) Lu, K.; Hu, Z.; Xiang, Z.; Ma, J.; Song, B.; Zhang, J.; Ma, H. Cation Intercalation in Manganese Oxide Nanosheets: Effects on Lithium and Sodium Storage. *Angewandte Chemie* **2016**, *128* (35), 10604-10608. DOI: 10.1002/ange.201605102.
- (29) Song, M.-S.; Lee, K. M.; Lee, Y. R.; Kim, I. Y.; Kim, T. W.; Gunjakar, J. L.; Hwang, S.-J. Porously Assembled 2D Nanosheets of Alkali Metal Manganese Oxides with Highly Reversible

- Pseudocapacitance Behaviors. *The Journal of Physical Chemistry C* **2010**, *114* (50), 22134-22140. DOI: 10.1021/jp108969s.
- (30) VahidMohammadi, A.; Liang, W.; Mojtabavi, M.; Wanunu, M.; Beidaghi, M. 2D Titanium and Vanadium Carbide MXene Heterostructures for Electrochemical Energy Storage. *Energy Storage Materials* **2021**, *41*, 554-562.
- (31) Chuanfang; Park, S.-H.; O'Brien, S. E.; Seral-Ascaso, A.; Liang, M.; Hanlon, D.; Krishnan, D.; Crossley, A.; McEvoy, N.; Coleman, J. N.; et al. Liquid Exfoliation of Interlayer Spacing-Tunable 2D Vanadium Oxide Nanosheets: High Capacity and Rate Handling Li-ion Battery Cathodes. *Nano Energy* **2017**, *39*, 151-161. DOI: 10.1016/j.nanoen.2017.06.044.
- (32) Coleman, J. N.; Lotya, M.; O'Neill, A.; Bergin, S. D.; King, P. J.; Khan, U.; Young, K.; Gaucher, A.; De, S.; Smith, R. J. Two-Dimensional Nanosheets Produced by Liquid Exfoliation of Layered Materials. *Science* **2011**, *331* (6017), 568-571.
- (33) Nicolosi, V.; Chhowalla, M.; Kanatzidis, M. G.; Strano, M. S.; Coleman, J. N. Liquid Exfoliation of Layered Materials. *Science* **2013**, *340* (6139), 1226419.
- (34) Houseman, L.; Mukherjee, S.; Andris, R.; Zachman, M. J.; Pomerantseva, E. Free-Standing Bilayered Vanadium Oxide Films Synthesized by Liquid Exfoliation of Chemically Preintercalated δ-Li_xV₂O₅·*n*H₂O. *Materials Advances* **2021**, *2* (8), 2711-2718. DOI: 10.1039/d1ma00085c.
- (35) Naguib, M.; Barsoum, M. W.; Gogotsi, Y. Ten Years of Progress in the Synthesis and Development of MXenes. *Advanced Materials* **2021**, *33* (39), 2103393. DOI: 10.1002/adma.202103393.
- (36) Stankovich, S.; Dikin, D. A.; Dommett, G. H. B.; Kohlhaas, K. M.; Zimney, E. J.; Stach, E. A.; Piner, R. D.; Nguyen, S. T.; Ruoff, R. S. Graphene-Based Composite Materials. *Nature* **2006**, 442 (7100), 282-286. DOI: 10.1038/nature04969.
- (37) Zhang, R.; Averianov, T.; Andris, R.; Zachman, M. J.; Pomerantseva, E. Liquid Phase Exfoliation of Chemically Prelithiated Bilayered Vanadium Oxide in Aqueous Media for Li-Ion Batteries. *The Journal of Physical Chemistry C* **2023**, *127* (2), 919-929. DOI: 10.1021/acs.jpcc.2c06875.
- (38) Created with BioRender.com.
- (39) Alonso, B.; Livage, J. Synthesis of Vanadium Oxide Gels from Peroxovanadic Acid Solutions: A 51V NMR Study. *Journal of Solid State Chemistry* **1999**, *148* (1), 16-19. DOI: 10.1006/jssc.1999.8283.
- (40) Konkena, B.; Vasudevan, S. Understanding Aqueous Dispersibility of Graphene Oxide and Reduced Graphene Oxide through p K_a Measurements. *The Journal of Physical Chemistry Letters* **2012**, *3* (7), 867-872. DOI: 10.1021/jz300236w.
- (41) Compton, O. C.; Nguyen, S. T. Graphene Oxide, Highly Reduced Graphene Oxide, and Graphene: Versatile Building Blocks for Carbon-Based Materials. *Small* **2010**, *6* (6), 711-723. DOI: 10.1002/smll.200901934.
- (42) Lu, G.; Ocola, L. E.; Chen, J. Reduced Graphene Oxide for Room-Temperature Gas Sensors. *Nanotechnology* **2009**, *20* (44), 445502.
- (43) Clites, M.; Hart, J. L.; Taheri, M. L.; Pomerantseva, E. Annealing-Assisted Enhancement of Electrochemical Stability of Na-Preintercalated Bilayered Vanadium Oxide Electrodes in Na-Ion Batteries. *ACS Applied Energy Materials* **2020**, *3* (1), 1063-1075. DOI: 10.1021/acsaem.9b02098. (44) Feng, H.; Cheng, R.; Zhao, X.; Duan, X.; Li, J. A Low-Temperature Method to Produce Highly Reduced Graphene Oxide. *Nature Communications* **2013**, *4* (1), 1539. DOI: 10.1038/ncomms2555.

- (45) Abello, L.; Husson, E.; Repelin, Y.; Lucazeau, G. Structural Study of Gels of V₂O₅: Vibrational Spectra of Xerogels. *Journal of Solid State Chemistry* **1985**, *56* (3), 379-389.
- (46) Ridley, P.; Gallano, C.; Andris, R.; Shuck, C. E.; Gogotsi, Y.; Pomerantseva, E. MXene-Derived Bilayered Vanadium Oxides with Enhanced Stability in Li-Ion Batteries. *ACS Applied Energy Materials* **2020**, *3* (11), 10892-10901. DOI: 10.1021/acsaem.0c01906.
- (47) Wang, Y.; Alsmeyer, D. C.; McCreery, R. L. J. C. o. M. Raman Spectroscopy of Carbon Materials: Structural Basis of Observed Spectra. **1990**, *2* (5), 557-563.
- (48) Scardaci, V.; Compagnini, G. Raman Spectroscopy Investigation of Graphene Oxide Reduction by Laser Scribing. C 2021, 7 (2), 48. DOI: 10.3390/c7020048.
- (49) Yang, D.; Velamakanni, A.; Bozoklu, G.; Park, S.; Stoller, M.; Piner, R. D.; Stankovich, S.; Jung, I.; Field, D. A.; Ventrice Jr, C. A. Chemical Analysis of Graphene Oxide Films After Heat and Chemical Treatments by X-Ray Photoelectron and Micro-Raman Spectroscopy. *Carbon* **2009**, *47* (1), 145-152.
- (50) Stobinski, L.; Lesiak, B.; Malolepszy, A.; Mazurkiewicz, M.; Mierzwa, B.; Zemek, J.; Jiricek, P.; Bieloshapka, I. Graphene Oxide and Reduced Graphene Oxide Studied by the XRD, TEM and Electron Spectroscopy Methods. *Journal of Electron Spectroscopy and Related Phenomena* **2014**, *195*, 145-154.
- (51) Mansour, A.; Dallek, S.; Smith, P.; Baker, W. Thermogravimetry and X-Ray Absorption Spectroscopy Study of Heated V₂O₅·nH₂O Aerogels and Ambigels. *Journal of The Electrochemical Society* **2002**, *149* (12), A1589.
- (52) Wu, Q.-H.; Thissen, A.; Jaegermann, W.; Liu, M. Photoelectron Spectroscopy Study of Oxygen Vacancy on Vanadium Oxides Surface. *Applied Surface Science* **2004**, *236* (1-4), 473-478.
- (53) Cohen, Y. S.; Aurbach, D. Surface Films Phenomena on Vanadium-Pentoxide Cathodes for Li and Li-Ion Batteries: *in situ* AFM Imaging. *Electrochemistry communications* **2004**, *6* (6), 536-542.
- (54) Koltypin, M.; Pol, V.; Gedanken, A.; Aurbach, D. The Study of Carbon-Coated V₂O₅ Nanoparticles as a Potential Cathodic Material for Li Rechargeable Batteries. *Journal of The Electrochemical Society* **2007**, *154* (7), A605.
- (55) Boukhalfa, S.; Evanoff, K.; Yushin, G. Atomic Layer Deposition of Vanadium Oxide on Carbon Nanotubes for High-Power Supercapacitor Electrodes. *Energy & Environmental Science* **2012**, *5* (5), 6872-6879.
- (56) Saraf, M.; Shuck, C. E.; Norouzi, N.; Matthews, K.; Inman, A.; Zhang, T.; Pomerantseva, E.; Gogotsi, Y. Free-Standing α-MoO₃/Ti₃C₂ MXene Hybrid Electrode in Water-in-Salt Electrolytes. *Energy & Environmental Materials* **2022**. DOI: 10.1002/eem2.12516.
- (57) Liu, Y.; Uchaker, E.; Zhou, N.; Li, J.; Zhang, Q.; Cao, G. Facile Synthesis of Nanostructured Vanadium Oxide as Cathode Materials for Efficient Li-Ion Batteries. *Journal of Materials Chemistry* **2012**, *22* (46), 24439. DOI: 10.1039/c2jm34078j.
- (58) Rahman, M. M.; Wang, J.-Z.; Idris, N. H.; Chen, Z.; Liu, H. Enhanced Lithium Storage in a VO₂(B)-Multiwall Carbon Nanotube Microsheet Composite Prepared via an *in situ* Hydrothermal Process. **2010**, *56* (2), 693-699. DOI: 10.1016/j.electacta.2010.10.012.
- (59) Liu, Y.; Liu, Q.; Li, Z.; Ren, Y.; Xie, J.; He, H.; Xu, F. Failure Study of Commercial LiFePO₄ Cells in Over-Discharge Conditions Using Electrochemical Impedance Spectroscopy. *Journal of The Electrochemical Society* **2014**, *161* (4), A620.

Table Of Contents Graphic

